Rapid Communications

Theoretical prediction of Weyl fermions in the paramagnetic electride Y_2C

Liangliang Liu,[1,2] Chongze Wang,[1] Seho Yi,[1] Dou Kyun Kim,[3] Chul Hong Park,[3] and Jun-Hyung Cho[1,*]

[1]*Department of Physics, Research Institute for Natural Science, HYU-HPSTAR-CIS High Pressure Research Center, Hanyang University, Seoul 133-791, Republic of Korea*

[2]*Key Laboratory for Special Functional Materials of Ministry of Education, Henan University, Kaifeng 475004, People's Republic of China*

[3]*Department of Physics Education, Pusan National University, Pusan 609-735, Republic of Korea*

(Received 22 January 2019; revised manuscript received 21 May 2019; published 6 June 2019)

Recent experimental observations of Weyl fermions in materials open a new frontier of condensed-matter physics. Based on first-principles calculations, we here discover the Weyl fermions in a two-dimensional (2D) layered electride material Y_2C. We find that the Y 4*d* orbitals and the anionic *s*-like orbital confined in the interstitial spaces between $[Y_2C]^{2+}$ cationic layers are hybridized to give rise to van Have singularities near the Fermi energy E_F, which induce a ferromagnetic (FM) order via the Stoner-type instability. This FM phase with broken time-reversal symmetry hosts the Weyl nodal lines near E_F, which are converted into the multiple pairs of Weyl nodes by including spin-orbit coupling. Furthermore, we find that Y_2C has a topologically nontrivial surface state near E_F as well as a tiny magnetic anisotropy energy, consistent with the observed surface state and paramagnetism at low temperatures below ~2 K. Our findings demonstrate the existence of Weyl fermions in a 2D electride material thereby providing a platform to study the interesting interplay of Weyl fermion physics and electride materials.

DOI: 10.1103/PhysRevB.99.220401

As an emerging class of low-dimensional electron systems, electrides have attracted considerable attention because of their promising prospects in both fundamental research and technological applications [1–4]. In electrides, the loosely bound electrons are easily separated from cationic atoms thereby being trapped in void spaces along one-dimensional channels [5,6] or between two-dimensional (2D) interlayers [7,8]. Such low-dimensional anionic electrons occupying the bands near the Fermi-level E_F may provide unconventional playgrounds for exploration of various exotic quantum phenomena, such as charge-density waves, spin ordering, superconductivity, and topological states [9–13]. Recently, Lee *et al.* demonstrated the synthesis of a layered electride material Ca_2N where the anionic electrons are distributed in the interlayer spaces between positively charged $[Ca_2N]^+$ cationic layers [14]. After such a pioneering realization of a 2D electride, extensive searches have been theoretically and experimentally carried out to find various types of 2D electride materials that offer the unique properties of high electrical conductivities [15], low work functions [16], highly anisotropic optical response [14], and efficient catalysts [17].

Among several existing 2D layered electrides, Y_2C containing two Y atoms and one C atom within the rhombohedral primitive unit cell [see Fig. 1(a)] shows a semimetallic feature with the electron and hole pockets near E_F [18]. Despite the recent intensive experimental and theoretical studies of Y_2C [18–27], its ground state has not yet been completely understood. Using a single-crystal Y_2C, Park *et al.* [23] reported the observation of a large magnetic anisotropy with a superior magnetic moment along the *c* axis where the effective magnetic moment μ_{eff} was estimated as $\sim 2.82\mu_B$ per Y atom. Meanwhile, some other experiments observed a paramagnetic phase in Y_2C even at low temperatures below ~2 K [19,20,22]. For examples, using single-crystal Y_2C samples, Otani *et al.* [20] observed a paramagnetic phase with weak magnetic anisotropy and $\mu_{eff} \approx 0.124\mu_B$ per Y atom, and Hiraishi *et al.* [22] observed a similar paramagnetic phase with weak magnetic anisotropy. For polycrystalline Y_2C samples, Zhang *et al.* [19] also measured the paramagnetic property with weak magnetic anisotropy and $\mu_{eff} \approx 0.604\mu_B$ per Y atom. However, such observed paramagnetism with weak magnetic anisotropy has not been properly explained by existing density-functional theory (DFT) calculations which were based on a nonmagnetic (NM) ground state [24–26] or a ferromagnetic (FM) ground state with large magnetic anisotropy [23]. Nevertheless, all theories [23–27] agree that there are highly localized charges or spins in the interstitial spaces between $[Y_2C]^{2+}$ cationic layers [see Fig. 1(b)].

In this Rapid Communication, based on first-principles calculations [28], we report that Y_2C behaves as paramagnetic with nearly degenerate FM Weyl semimetal states. By analyzing the electronic structures of few-layer and bulk Y_2C, we find that the FM phase begins to be stabilized from bilayer Y_2C via the Stone-type instability, indicating that the confined anionic electrons between the two $[Y_2C]^{2+}$ cationic layers are associated with the appearance of FM spin ordering. For bulk Y_2C, the hybridization of Y 4*d* orbitals and anionic *s*-like orbital produces small orbital angular momenta, which, in turn, contribute to a magnetic anisotropy energy (MAE) of several μeV per unit cell. This extremely small MAE invokes FM fluctuations which can provide an explanation for the experimental observation [19,20,22] of paramagnetism even at ~2 K. Remarkably, the electronic structure of the FM phase

*Corresponding author: chojh@hanyang.ac.kr

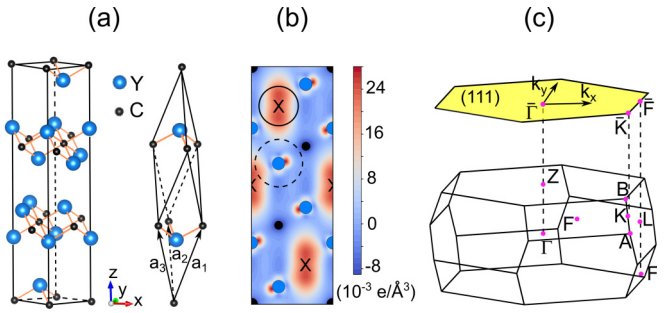

FIG. 1. (a) Optimized structure of bulk Y_2C within the trigonal conventional cell (left) and rhombohedral primitive cell (right), (b) spin density plotted on the (110) face of the conventional cell, and (c) Brillouin zone (BZ) of the rhombohedral primitive cell together with the projected surface BZ of the (111) surface. In (b), "X" denotes the central region of localized anionic electrons, and the dashed (solid) circle represents the sphere of radius 1.82 (1.50) Å around the Y (X) atom.

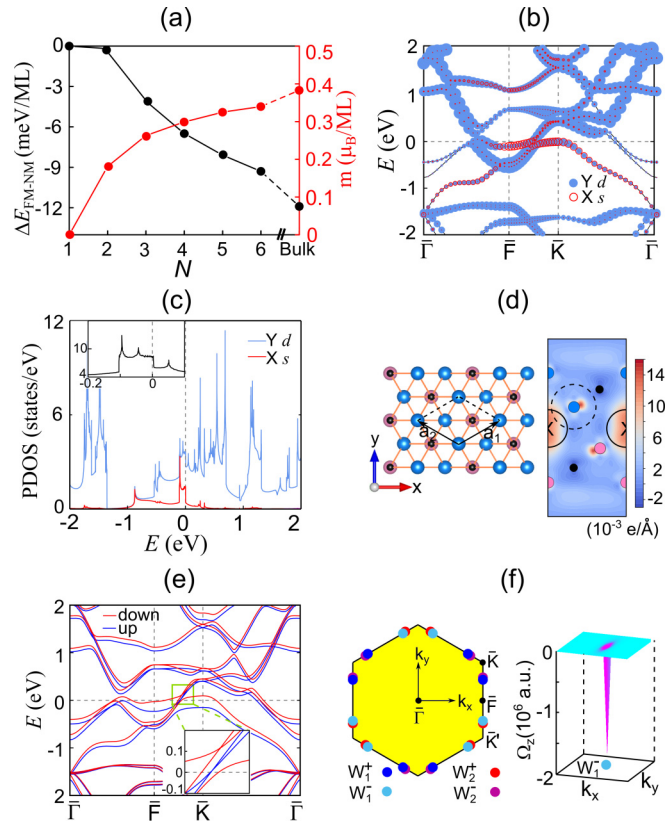

FIG. 2. (a) Calculated energy difference $\Delta E_{\text{FM-NM}}$ and magnetic moments m of the FM phase as a function of N. For bilayer Y_2C, the calculated band structure and partial DOS (PDOS) of the NM phase are displayed in (b) and (c), respectively. In (b), the bands projected onto the Y d and X s orbitals are displayed with circles whose radii are proportional to the weights of the corresponding orbitals. The energy zero represents E_F. A closeup of the total DOS near E_F is given in the inset of (c). The structure (top view) and spin density of bilayer Y_2C is drawn in (d) where the blue and pink circles represent the first- and second-layer Y atoms. The band structure for the FM phase of bilayer Y_2C is given in (e) together with the zoom-in band structure along the $\overline{FK}$ line. In (f), three nonequivalent pairs of Weyl nodes for each spin channel are drawn in the BZ, and the distribution of the Berry curvature component Ω_z around W_1^- is displayed.

shows the existence of the Weyl nodal lines (WNLs) near E_F, which are converted into the multiple pairs of Weyl nodes by including spin-orbit coupling (SOC). In particular, we identify a drumheadlike surface state near E_F, the dispersion of which is insensitive to the positions of Weyl nodes varying with respect to the magnetization direction. This topologically nontrivial surface state is corroborated by a previous angle-resolved photoemission spectroscopy (ARPES) measurement [18]. Thus, our findings not only solve the outstanding discrepancy between experiment and theory regarding the ground state of Y_2C, but also illustrate the exploration of Weyl fermions whose Brillouin-zone coordinates fluctuate in momentum space.

We begin by examining the relative stability of the FM and NM phases in few-layer Y_2C with increasing the number N of layers. Figure 2(a) shows the calculated energy difference $\Delta E_{\text{FM-NM}}$ between the FM and the NM phases as a function of N. We find that a monolayer (ML) Y_2C ($N = 1$) has the NM ground state, whereas few-layer Y_2C with $N \geqslant 2$ have the FM one. It is noted that, for $N = 2$, the FM ground state is more stable than the antiferromagnetic state by ~0.5 meV per ML (see Fig. S1 of the Supplemental Material [34]). In Fig. 2(a), the calculated magnetic moment m of the FM phase is also displayed with respect to N. It is seen that m increases monotonously with increasing N, being saturated to be 0.383 μ_B/ML at bulk Y_2C [35]. To explore the underlying mechanism of the FM order, we calculate the band structure and the density of states (DOS) for the NM phase of bilayer ($N = 2$) and bulk Y_2C. For $N = 2$, the calculated band structures exhibit the electron (hole) pocket around the $\overline{F}$ ($\overline{K}$) point near E_F [see Fig. 2(b)], producing the van Have singularities (vHs) with a large total DOS [see the inset of Fig. 2(c)]. Consequently, the FM order is induced via Stoner criterion $D(E_F)I > 1$ [36] (see Fig. S2 of the Supplemental Material [34]), where $D(E_F)$ is the total DOS at E_F, and the Stoner parameter I can be estimated with dividing the exchange splitting of spin-up and spin-down bands by the corresponding magnetic moment.

It is noteworthy that, for bilayer Y_2C, the PDOS projected onto the Y 4d orbitals and the anionic s-like orbital confined in the interstitial regions between the two $[Y_2C]^{2+}$ cationic layers exhibits sharp peaks close to E_F [see Fig. 2(c)], indicating a strong hybridization of the two orbitals. Compared to other orbitals, these two orbitals are found to be more dominant components of the electron- and hole-pocket states near E_F: See the band projections in Fig. S3 of the Supplemental Material [34]. Due to such a hybridization of the Y 4d and anionic s-like orbitals, the spin densities for bilayer and bulk Y_2C are distributed over the Y atoms and the interstitial regions X as shown in Figs. 2(d) and 1(b), respectively. For bilayer (bulk) Y_2C, the calculated spin moments integrated within the spheres around Y and X [see Figs. 2(d) and 1(b)] are 0.043 (0.108) and 0.088 (0.169)μ_B, respectively. Based on our results, we can say that, for $N \geqslant 2$ and bulk Y_2C, the vHs arising from the electron and hole pockets with the

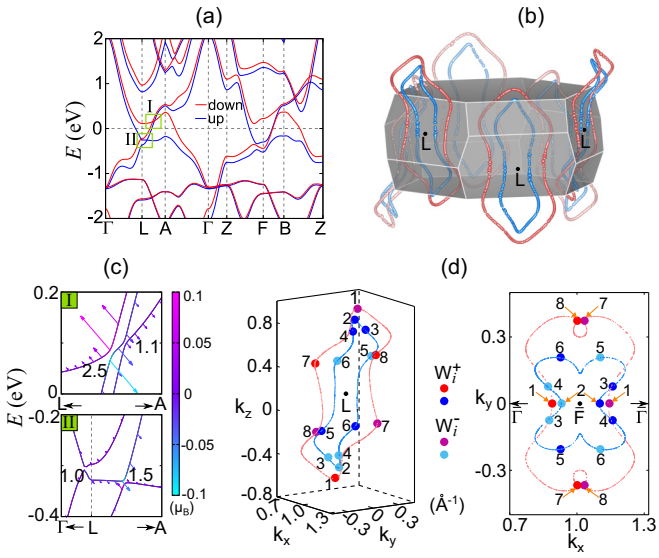

FIG. 3. (a) Band structure and (b) WNLs of the FM phase of bulk Y_2C, computed in the absence of SOC. The closeup band structures around regions I and II, computed with including SOC, are given in (c). Here, the arrows along the horizontal and vertical directions represent the m_x and m_y components, respectively, whereas the arrow colors indicate m_z. The values m_x, m_y, and m_z for the longest arrow are -0.117, 0.067, and $0.109\mu_B$, respectively. In (c), the numbers represent the SOC-induced gap (in meV) at several $\mathbf{k}$ points. In (d), the distribution of Weyl nodes is drawn in the three-dimensional (left) and 2D (right) views.

hybridization of the Y $4d$ and anionic s-like orbitals cause the Stoner-type instability to induce an FM spin ordering.

Figure 2(e) shows the band structure for the FM phase of bilayer Y_2C. We find that there exist two spinful Weyl nodes just above E_F along the $\overline{FK}$ line [see the inset of Fig. 2(e)]. It is noted that the crystalline symmetries of bilayer Y_2C represent the point-group D_{3d}, which contains inversion symmetry P, threefold rotational symmetry C_{3z} about the z axis, and twofold rotation symmetry C_{2y} about the y axis. Therefore, for each spin channel, we have three nonequivalent pairs of Weyl nodes along the $\overline{FK}$ and $\overline{FK'}$ lines [see Fig. 2(f)] where each Weyl node at a point $\mathbf{k}$ is paired with the other Weyl node of opposite chirality at $-\mathbf{k}$ [37,38]. Note that the twofold degeneracy of such 2D Weyl nodes in the $\overline{FK}$ and $\overline{FK'}$ lines is mandated by C_{2y} rotation [38]: i.e., two crossing bands have opposite eigenvalues ±1 of C_{2y}. In order to verify these Weyl nodes, we calculate the Berry curvature around the band touching points by using the WANNIERTOOLS package [39]. Here, the Wannier bands are in good agreement with the first-principles bands (see Fig. S4 of the Supplemental Material [34]). It is found that each pair of Weyl nodes have the positive and negative Berry curvature distributions [see Fig. 2(f)], which can be regarded as the source and sink of Berry curvature in momentum space, respectively.

It is interesting to examine how the Weyl nodes in bilayer Y_2C evolve as such 2D Weyl semimetal is stacked into bulk Y_2C. Figure 3(a) shows the band structure for the FM phase of bulk Y_2C. Similar to bilayer Y_2C, there are two spinful Weyl nodes along the $\overline{LA}$ line (parallel to $\overline{FK}$ in 2D BZ), which, in turn, form closed nodal loops around the L points [see Fig. 3(b)]. The presence of such nodal loops with large deformation along the k_z direction implies strong interlayer couplings between cationic layers through anionic electrons, contrasting with small deformed nodal lines reported in layered materials with weak van der Waals interlayer couplings [40]. Since the crystalline symmetries of bulk Y_2C belong to the space-group $R\bar{3}m$ (No. 225) with the point-group D_{3d}, there are three separate WNLs for each spin channel. We note that the spinless nodal lines or Dirac nodal lines (DNLs) in nonmagnetic Y_2C are protected by spatial inversion (P) and time-reversal (T) symmetry [26]. Due to the broken T symmetry in the FM phase, these DNLs split into two spinful WNLs [see Fig. 3(b)]. To confirm the symmetry protection of WNLs, we introduce various perturbations of the Y atoms which break or preserve P and three nonequivalent C_2 rotation symmetries. Our calculated DFT and Wannier bands show a gap opening of the WNLs only for the P-symmetry-breaking geometries (see Fig. S5 of the Supplemental Material [34]). We further demonstrate the topological characterization of the WNLs by calculating the topological index [41], defined as $\zeta_1 = \frac{1}{\pi}\oint_c dk\, A(k)$, along a closed loop encircling any of the WNLs. Here, $A(k) = -i\langle u_k|\partial_k|u_k\rangle$ is the Berry connection of the related Bloch bands. We obtain $\zeta_1 = \pm1$ for the WNLs, indicating that they are stable against P symmetry conserving perturbations.

So far, we have considered the band structures in the absence of SOC where two spin channels in the FM phase are decoupled from each other because of the independence of the spin and orbital degrees of freedom. However, the inclusion of SOC lifts the degeneracy at the band-crossing points along the $\overline{LA}$ line as shown in Fig. 3(c). Each spin-up (spin-down) WNL in Fig. 3(b) becomes gapped with the exception of three (five) pairs of Weyl nodes [see Fig. 3(d)]. The positions of Weyl nodes in momentum space are given in Table SI of the Supplemental Material [34] together with their energies. Here, the spontaneous magnetization direction is calculated to be along the z axis, consistent with the experimental measurement of anisotropic magnetic properties [23]. The corresponding magnetic point group is C_{3i} containing P, C_{3z} about the z axis, as well as the product $C_{2y}T$ of rotation C_{2y} and time-reversal T. Therefore, the WNLs with three nonequivalent C_2 symmetries are not allowed anymore, leading to the opening of SOC gaps depending on unquenched orbital magnetic moments [see Fig. 3(c)]. As shown in Fig. 3(d), each pair of Weyl nodes associated with inversion P has its counterpart through $C_{2y}T$ symmetry: e.g., (W_3^+, W_3^-) and (W_4^+, W_4^-). Note that such counterparts of (W_1^+, W_1^-) and (W_2^+, W_2^-) are themselves.

Figure 4(a) plots the FM band structure along the M-L-M_1 line involving the W_1^+ and W_1^- nodes of positive and negative chiralities, respectively. The 2D views of Berry curvature around W_1^+ and W_1^- are displayed in Fig. 4(b). We determine the chirality of each Weyl node by integrating the Berry curvature through a closed 2D manifold enclosing the node. The computed chirality (i.e., the Chern number) is $C = +1$ and -1 for W_1^+ and W_1^-, respectively. Since the hallmark of Weyl nodes is the existence of topologically protected surface states, we calculate the surface electronic structure of Y_2C using the Green's function method based on the

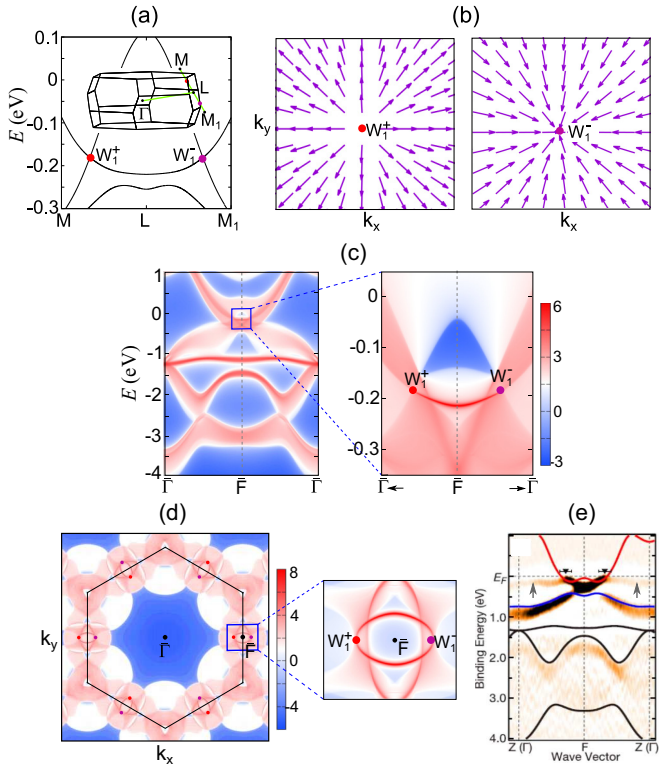

FIG. 4. (a) FM band structure of bulk Y_2C along the M-L-M_1 line, (b) Berry curvature around W_1^+ and W_1^-, and (c) projected surface spectrum for the (111) surface of Y_2C with a closeup image around the $\overline{F}$ point. The isoenergy surface at -0.183 eV below E_F is displayed in (d). Experimental band structure [18] obtained by plotting the second derivative of the ARPES spectra (Copyright ©2017 American Physical Society) is given in (e).

tight-binding Hamiltonian with maximally localized Wannier functions [39,42]. Figure 4(c) shows the projected surface spectrum on the (111) surface of Y_2C. Obviously, we find a topological surface state connecting two Weyl nodes W_1^+ and W_1^- around the $\overline{F}$ point. In Fig. 4(d), we plot the projected Fermi surface of the (111) surface, obtained at a chemical potential of -0.183 eV below E_F. A closeup of this Fermi surface represents two Fermi arcs connecting the W_1^+ and W_1^- nodes, showing the same shape as the drumhead surface state in the WNL semimetal state obtained without SOC (see Fig. S6(a) of the Supplemental Material [34]). Note that this drumhead shape remains invariant as the chemical potential is lowered up to -0.215 eV [see Fig. S6(b)]. It is thus likely that the small SOC-induced gap openings [see Fig. 3(c)] along the WNLs except at the Weyl nodes hardly change the dispersion of the drumhead surface state [38].

In Fig. 4(e), the ARPES data [18] obtained from the paramagnetic phase exhibits a strong intensity around the $\overline{F}$ point between the partially occupied and the fully occupied bands near E_F [43]. Such an observed in-gap state agrees well with the present FM topological surface state [see Fig. 4(c)]. This may imply that the dispersion of the topologically nontrivial surface state around the $\overline{F}$ point would be insensitive to the magnetization direction as demonstrated below. It is noted that the observed in-gap state was interpreted [26] in terms of a topological surface state originating from the topological property of Z_2 invariant in bulk Y_2C. However, there are the different features of the surface states between the Z_2-topological surface state and the present FM topological surface state. Contrasting the latter surface state connecting the two Weyl nodes W_1^+ and W_1^-, the former surface state shows the existence of the Dirac cone around the $\overline{F}$ point (see Fig. S9).

As indicated by the arrows in Fig. 4(e), the ARPES data exhibits another surface state around the $\overline{\Gamma}$ point below E_F with relatively weaker intensity. Although this surface state is absent in the surface spectral function of Fig. 4(c), it can be reproduced by the present [see Figs. S7(a)] and previous [13,25] DFT calculations which take the local surface potential modification into account. To examine the topological features of the two surface states around the $\overline{\Gamma}$ and $\overline{F}$ points, we passivate the $Y_2C(111)$ surface with H atoms. Using a slab of $N = 15$, we compare the calculated band structures of a clean $Y_2C(111)$ surface and the H-passivated $Y_2C(111)$ surface. As shown in Figs. S7(a) and S7(b), we find that, upon H adsorption, the surface state around the $\overline{\Gamma}$ point below E_F disappears due to the formation of Y-H bonds, whereas that around the $\overline{F}$ point still exists near E_F. Thus, the surface states around the $\overline{\Gamma}$ and $\overline{F}$ points are likely to be characterized as being topologically trivial and nontrivial, respectively [44,45].

In order to explain why experiments have not observed ferromagnetism even at low temperatures below ~2 K [19,20,22], we calculate the MAE for bulk Y_2C. We find that the magnetic configuration with the magnetization direction along the z axis is more favorable than that along the x axis by ~8 μeV per unit cell [35], indicating that the two magnetic configurations are nearly degenerate. This extremely small MAE provides an explanation for the experimentally observed paramagnetism at low temperatures below ~2 K [19,20,22]. It is noted that most of the experimentally [19,20,22] measured magnetic susceptibilities χ exhibited the paramagnetic behaviors in a wide range of temperature between ~1 and 300 K. However, since the measured magnetic susceptibilities of Y_2C showed strong sample-to-sample variations [19,20,22,23], further investigations of the detailed characterization of the paramagnetic phase are demanded in the future. We also find that the calculated orbital magnetic moments are two orders smaller in magnitude than spin moments (see Table SII of the Supplemetal Material [34]), leading to a very weak SOC that is consistent with the experimental observation of no obvious magnetic anisotropy [20,22]. It is noteworthy that, although the positions of Weyl nodes change depending on the magnetization direction, such Weyl semimetal states exhibit similar dispersions of the surface states connecting the corresponding Weyl nodes around the $\overline{F}$ point, which are also close to that of the drumheadlike surface state in the WNL state. Thus, we can say that the dispersion of the paramagnetic surface state [see Fig. 4(e)], measured by a previous ARPES experiment [18], nearly coincides with that of the topologically nontrivial drumhead surface state generated from the WNL semimetal state.

To conclude, based on first-principles calculations, we have predicted new FM Weyl semimetal states in a 2D layered electride material Y_2C. By a systematic study of the electronic structures of few-layer and bulk Y_2C, we identified that the

hybridization of the Y d orbitals and the anionic s-like orbital confined between the two $[Y_2C]^{2+}$ cationic layers comprises the vHs near E_F, therefore, inducing an FM spin ordering to produce a Weyl semimetal. In particular, it is revealed that, due to its small SOC effects, Y_2C has not only a drumheadlike surface state near E_F characterizing a WNL semimetal, but also a tiny magnetic anisotropy to invoke FM fluctuations, providing an explanation for the observed topologically nontrivial surface state and paramagnetism at ~2 K. The present exploration of Weyl fermions hidden in an apparent paramagnetic electride Y_2C manifests the intriguing combination of topology and electride materials. By applying an external magnetic field which can easily switch the magnetization direction of Y_2C, it is possible not only to realize the emergence of FM Weyl semimetal states, but also to tune the positions of Weyl nodes. Interestingly, since the lanthanide carbides, such as Gd_2C Tb_2C, Dy_2C, Ho_2C, and Er_2C [24] have shown the same/similar FM order, crystalline symmetries, and semimetal band dispersions as those of Y_2C, we anticipate that the emergence of FM Weyl semimetal states can be generic to all these lanthanides.

This Rapid Communication was supported by a National Research Foundation of Korea (NRF) grant funded by the Korean Government (Grants No. 2019R1A2C1002975, No. 2016K1A4A3914691, and No. 2015M3D1A1070609). The calculations were performed by the KISTI Supercomputing Center through the Strategic Support Program (Program No. KSC-2018-CRE-0063) for the supercomputing application research and by the High Performance Computational Center of Henan University.

L.L., C.W., and S.Y. contributed equally to this work.

[1] L. Li, C. Richter, J. Mannhart, and R. C. Ashoori, Nat. Phys. **7**, 762 (2011).
[2] C. J. Pickard and R. J. Needs, Nature Mater. **9**, 624 (2010).
[3] H. Lee, N. Cambell, J. Lee, T. J. Asel, T. R. Paudel, H. Zhou, J. W. Lee, B. Noesges, J. Seo, B. Park, L. J. Brillson, S. H. Oh, E. Y. Tsymbal, M. S. Rzchowski, and C. B. Eom, Nature Mater. **17**, 231 (2018).
[4] N. Boudjada, G. Wachtel, and A. Paramekanti, Phys. Rev. Lett. **120**, 086802 (2018).
[5] C. Park, S. W. Kim, and M. Yoon, Phys. Rev. Lett. **120**, 026401 (2018).
[6] T. Pandey, C. A. Polanco, V. R. Cooper, D. S. Parker, and L. Lindsay, Phys. Rev. B **98**, 241405(R) (2018).
[7] S. Zhao, Z. Li, and J. Yang, J. Am. Chem. Soc. **136**, 13313 (2014).
[8] S. Yi, J. H. Choi, K. Lee, S. W. Kim, C. H. Park, and J. H. Cho, Phys. Rev. B **94**, 235428 (2016).
[9] G. Grüner, *Density Waves in Solids* (Perseus, Cambridge, MA, 1994).
[10] J. R. Tolsma, M. Polini, and A. H. MacDonald, Phys. Rev. B **95**, 205101 (2017).
[11] Z. Wan, A. Kazakov, M. J. Manfra, L. N. Pfeiffer, K. W. West, and L. P. Rokhinson, Nat. Commun. **6**, 7426 (2015).
[12] S.-C. Zhu, L. Wang, J. Qu, J. Wang, T. Frolov, X. Q. Chen, and Q. Zhu, Phys. Rev. Mater, **3**, 024205 (2019).
[13] M. Hirayama, S. Matsuishi, H. Hosono, and S. Murakami, Phys. Rev. X **8**, 031067 (2018).
[14] K. Lee, S. W. Kim, Y. Toda, S. Matsuishi, and H. Hosono, Nature (London) **494**, 336 (2013).
[15] J. L. Dye, Science **301**, 607 (2003).
[16] W. Ming, M. Yoon, M. H. Du, K. Lee, and S. W. Kim, J. Am. Chem. Soc. **138**, 15336 (2016).
[17] M. Kitano, Y. Inoue, Y. Yamazaki, F. Hayashi, S. Kanbara, S. Matsuishi, T. Yokoyama, S. Kim, M. Hara, and H. Hosono, Nat. Chem. **4**, 934 (2012).
[18] K. Horiba, R. Yukawa, T. Mitsuhashi, M. Kitamura, T. Inoshita, N. Hamada, S. Otani, N. Ohashi, S. Maki, J. I. Yamaura, H. Hosono, Y. Murakami, and H. Kumigashira, Phys. Rev. B **96**, 045101 (2017).
[19] X. Zhang, Z. Xiao, H. Lei, Y. Toda, S. Matsuishi, T. Kamiya, S. Ueda, and H. Hosono, Chem. Mater. **26**, 6638 (2014).
[20] S. Otani, K. Hirata, Y. Adachi, and N. Ohashi, J. Cryst. Growth **454**, 15 (2016).
[21] J. Park, J. Y. Hwang, K. H. Lee, S. G. Kim, K. Lee, and S. W. Kim, J. Am. Chem. Soc. **139**, 17277 (2017).
[22] M. Hiraishi, K. M. Kojima, I. Yamauchi, H. Okabe, S. Takeshita, A. Koda, R. Kadono, X. Zhang, S. Matsuishi, H. Hosono, K. Hirata, S. Otani, and N. Ohashi, Phys. Rev. B **98**, 041104(R) (2018).
[23] J. Park, K. Lee, S. Y. Lee, C. N. Nandadasa, S. Kim, K. H. Lee, Y. H. Lee, H. Hosono, S. G. Kim, and S. W. Kim, J. Am. Chem. Soc. **139**, 615 (2017).
[24] T. Inoshita, S. Jeong, N. Hamada, and H. Hosono, Phys. Rev. X **4**, 031023 (2014).
[25] T. Inoshita, S. Takemoto, T. Tada, and H. Hosono, Phys. Rev. B **95**, 165430 (2017).
[26] H. Huang, K.-H. Jin, S. Zhang, and F. Liu, Nano Lett. **18**, 1972 (2018).
[27] T. Inoshita, N. Hamada, and H. Hosono, Phys. Rev. B **92**, 201109(R) (2015).
[28] The present DFT calculations were performed using the Vienna *ab initio* simulation package with the projector-augmented wave (PAW) method [29,30,31]. For the exchange-correlation energy, we employed the generalized-gradient approximation functional of Perdew-Burke-Ernzerhof (PBE) [32]. The inclusion of van der Waals interactions was considered using the PBE-D3 scheme [33]. The ML and bilayer were modeled by a periodic slab geometry with ~30 Å of vacuum in between the slabs. For bulk Y_2C, the adjacent three Y_2C layers are stacked in an ABC-type trilayer pattern along the z direction as shown in Fig. 1(a). A plane-wave basis was employed with a kinetic-energy cutoff of 600 eV, and the **k**-space integration was performed with the 21×21 and 21×21×21 meshes in the Brillouin zones of ML (or few layer) and bulk, respectively. All atoms were allowed to relax along the calculated forces until all the residual force components were less than 0.005 eV/Å.
[29] G. Kresse and J. Hafner, Phys. Rev. B **48**, 13115 (1993).
[30] G. Kresse and J. Furthmüller, Comput. Mater. Sci. **6**, 15 (1996).
[31] P. E. Blöchl, Phys. Rev. B **50**, 17953 (1994).

[32] J. P. Perdew, K. Burke, and M. Ernzerhof, Phys. Rev. Lett. **77**, 3865 (1996); **78**, 1396 (1997).

[33] S. Grimme, J. Antony, S. Ehrlich, and H. Krieg, J. Chem. Phys. **132**, 154104 (2010).

[34] See Supplemental Material at http://link.aps.org/supplemental/10.1103/PhysRevB.99.220401 for the antiferromagnetic configurations, the band structures, and DOS for the NM phase of bulk Y_2C, the band projections onto all the Y, C, and interstitial X orbitals of bilayer Y_2C, the Wannier bands, and the drumhead surface state.

[35] Our calculated values of $\Delta E_{\text{FM-NM}}$ and m agree well with those ($\Delta E_{\text{FM-NM}} = -12$ meV and $m = 0.36\mu_B$ per primitive unit cell) obtained from a previous all-electron calculation (see Table I in Ref. [27]). Therefore, we expect that the MAE obtained using the presently employed PAW method and the all-electron full potential linearized augmented plane-wave method would be close to each other. In addition, we use the PBE + U method to calculate the MAE. Here, we consider an on-site Coulomb interaction of $U = 2$ eV for the Y $4d$ orbitals. The calculated PBE + U value of MAE is $\sim$4 μeV per unit cell, which is smaller than that (μeV per unit cell) obtained from the PBE calculation.

[36] H. L. Zhuang, P. R. C. Kent, and R. G. Hennig, Phys. Rev. B **93**, 134407 (2016).

[37] M. Yao, H. Lee, N. Xu, Y. Wang, J. Ma, O. V. Yazyev, Y. Xiong, M. Shi, G. Aeppli, and Y. Soh, arXiv:1810.01514.

[38] Y. J. Jin, R. Wang, Z. J. Chen, J. Z. Zhao, Y. J. Zhao, and H. Xu, Phys. Rev. B **96**, 201102(R) (2017).

[39] Q. Wu, S. Zhang, H.-F. Song, M. Troyer, and A. A. Soluyanov, Comput. Phys. Commun. **224**, 405 (2018).

[40] S. Nie, H. Weng, and F. B. Prinz, Phys. Rev. B **99**, 035125 (2019).

[41] C. Fang, H. Weng, X. Dai, and Z. Fang, Chin. Phys. B **25**, 117106 (2016).

[42] A. A. Mostofi, J. R. Yates, Y.-S. Lee, I. Souza, D. Vanderbilt, and N. Marzari, Comput. Phys. Commun. **178**, 685 (2008).

[43] In Fig. 4(e), the second derivative of the ARPES spectra show that the observed intensity of the blue-line band along the Z-F-Z direction [see Figs. 2(d) and 3(a) in Ref. 18] is broadened up to $\sim$0.4 eV, which is larger than the spin splitting $\sim$0.15 eV of the FM bands along the Z-F line [see Fig. 3(a)]. Therefore, the FM spin-split bands are unlikely to be resolved by the ARPES spectra of Ref. [18].

[44] H. M. Benia, C. Lin, K. Kern, and C. R. Ast, Phys. Rev. Lett. **107**, 177602 (2011).

[45] F. Virot, R. Hayn, M. Richter, and J. van den Brink, Phys. Rev. Lett. **111**, 146803 (2013).